# **Manuscript Template**

Forecasting mechanical failure and the June 26, 2018 eruption of Sierra Negra Volcano, Galápagos - Ecuador

Patricia M. Gregg<sup>1</sup>\*, Yan Zhan<sup>2</sup>, Falk Amelung<sup>3</sup>, Dennis Geist<sup>4,5</sup>, Patricia Mothes<sup>6</sup>, Seid Koric<sup>7,8</sup>, Zhang Yunjun<sup>9</sup>

- <sup>1</sup>Department of Geology, School of Earth, Society, and Environment, University of Illinois, Urbana, IL, USA
- <sup>2</sup> Earth and Planets Laboratory, Carnegie Institution for Science, Washington, DC, USA
- <sup>3</sup> Department of Marine Geosciences, Rosenstiel School of Marine and Atmospheric Sciences, University
   of Miami, FL, USA
- <sup>4</sup>Division of Earth Sciences, National Science Foundation, Alexandria, VA, USA
  - <sup>5</sup> Department of Geology, Colgate University, Hamilton, NY, USA
  - <sup>6</sup> Instituto Geofísico, Escuela Politécnica Nacional, Quito, Ecuador
- <sup>7</sup> National Center for Supercomputing Applications, University of Illinois, Urbana, IL, USA
- <sup>8</sup> Mechanical Science and Engineering, University of Illinois, Urbana, IL, USA
- <sup>9</sup> Seismological Laboratory, California Institute of Technology, Pasadena, CA, USA

\*Corresponding Author: Patricia M. Gregg (pgregg@illinois.edu)

## **Abstract** (<150 words)

Utilizing recent advancements in high performance computing data assimilation to combine satellite InSAR data with numerical models, the prolonged unrest of Sierra Negra volcano in the Galápagos was tracked to provide a fortuitous, but successful, forecast five months in advance of the June 26, 2018 eruption. Subsequent numerical simulations reveal that the evolution of the stress state in the host rock surrounding the Sierra Negra magma system likely controlled eruption timing. While changes in magma reservoir pressure remained modest (< 15 MPa), modeled widespread Mohr-Coulomb failure is coincident with the timing of the June 26, 2018 Mw 5.4 earthquake and subsequent eruption. Coulomb stress transfer models suggest that the faulting event triggered the 2018 eruption by encouraging tensile failure along the northern portion of the caldera. These findings provide a critical framework for understanding Sierra Negra's eruption cycles and evaluating the potential and timing of future eruptions.

#### Introduction

One of the great challenges in the field of volcanology is to develop quantitative models to investigate the processes that lead to volcanic eruptions and use these models to provide eruption forecasts (1). Meeting this challenge requires the development of models capable of interpreting field observations and tracking the evolution of a magma system. One widely used, observation of volcanic unrest is ground deformation. As magma accumulates in a subsurface reservoir the overlying ground surface above it swells (2). The surface signal, captured by satellite or ground measurements, can be inverted to estimate volume changes in a burried magma source. Deformation signals often begin months to years prior to an eruption, providing early warning of volcanic activity (3). However, linking a

surface deformation signal to eruption likelihood is challenging, and frequently the magnitude of the signal does not provide an accurate indication of eruption potential or timing (4). In particular, volcano inflation does not always lead to an eruption and eruptions can occur when no preceding surface displacement is detected (5). As such, short-term observations, such as changes in seismicity on the timescales of minutes to hours, have typically been more successful predictors of an impending eruption (6). However, clear signals are often lacking (e.g., the lack of seismic precursors at many Aleutian volcanoes (7) or the lack of precursory deformation at open volcanic systems (8)), making eruption forecasting difficult.

565758

59

60 61

62 63

64

65

66 67

68

69

70

71 72

73

74

Multiphysics-based numerical modeling approaches provide a means for investigating eruption catalysts by calculating the evolution of the host rock stress and reservoir pressure during periods of unrest (9, 10). A critical advancement is combining these models with geophysical observations to track a system's evolution in real time. Model-data fusion frameworks, often used in climate modeling (11), are key for investigating how a system evolves. The Ensemble Kalman Filter (EnKF), an ensemble-based Markov chain Monte Carlo (MCMC) sequential data assimilation approach (12), has recently been adapted for tracking volcano system evolution (13-15). The EnKF has shown great promise for assimilating large geospatial data, such as Interferometric Synthetic Aperture Radar (InSAR) satellite and ground-based Global Navigation Satellite System (GNSS) deformation data, into multiphysics volcano finite element method (FEM) models (16). The high-performance computing, EnKF approach provides updates of the volcano system state through time, including an estimation of host rock stress, failure, and magma reservoir pressure. Estimations of stress and failure provide insight into the stability of a magma system and potential triggering mechanisms for magma migration and eruption, which is particularly beneficial in the absence of clear precursors (16).

75 76 77

78

79

80

81

82

83

84

85

86

87

88

89

90

91

92

Sierra Negra, the most voluminous of the Galápagos volcanoes, is a 60x40 km basaltic shield volcano that occupies most of the southern portion of Isabela Island (Fig. 1) (17). Sierra Negra has experienced at least 7 historic eruptions since 1911. with an eruption occurring approximately every 15 years (17, 18). Sierra Negra's prolonged, inter-eruption cycle with extensive uplift and seismicity provides a unique natural laboratory to investigate stress evolution of a volcano and potential eruption precursors and catalysts while testing the EnKF approach. Sierra Negra experienced an extended period of unrest prior to its two most recent eruptions (in 2005 and 2018. Preceding its 2005 eruption, caldera-centered uplift > 5 m was observed, culminating in a M<sub>w</sub> 5.5 earthquake on the trapdoor fault system in the southern caldera floor followed within hours by an eruption on October 22, 2005 (18, 19). By the spring of 2018, the magnitude of the observed inflation since 2005 had reached 6.5 m (20, 21). The June 26, 2018 eruption commenced at 1340 LT and was preceded by a rapid increase in seismicity including a M<sub>w</sub> 5.4 event that struck at 0315 LT, also along the southern side of the caldera trapdoor fault system (Fig. 1) (20, 22). The 2018 eruption lasted for 58 days and covered a 30.6 km<sup>2</sup> area in fresh lava flows (22).

93 94 95

96

97

Several questions surround the protracted unrest periods observed at Sierra Negra, including how its magma system endures such significant and rapid inflation prior to eruption. Previous studies have pointed to the release of stress accumulated due

to magma intrusion by slip along trapdoor faults in the overlying roof (19, 23-25) and the ductile nature of the warm host rock limiting stress accumulation near the reservoir (10). These hypothesized mechanisms for stress relief and the rheological buffering of eruption-driving failure accumulation make Sierra Negra both a challenging and attractive target for testing new volcano forecasting techniques.

In this investigation, the EnKF approach is used to evaluate the large-magnitude uplift observed at Sierra Negra volcano leading up to its June 26, 2018 eruption. In January 2018, five months prior to the eruption an initial EnKF forecast for Sierra Negra was completed utilizing selected Sentinel-1 InSAR observations from 2014-2018. The forecast indicated that an eruption was likely to occur between June 25, 2018 and July 5, 2018 due to the significant and widespread accumulation of brittle failure in the host rock surrounding the magma reservoir. After the 2018 eruption, additional EnKF experiments were conducted using additional InSAR deformation data to evaluate the success of the pre-eruption forecast and provide strategies for conducting future forecasts. This paper explores how the January 2018 forecast for Sierra Negra was both a lucky accident and an encouraging sign for transformative advances in volcano forecasting. The primary goals of this study are: (1) to evaluate the eruption precursor signals and eruption triggering mechanisms at Sierra Negra; and (2) assess the ability of the EnKF approach to accurately track and forecast the system state through time.

#### Results

In the EnKF analysis presented here, an ensemble containing 240 three-dimensional FEM models was updated sequentially through time as new InSAR observations became available. Each of the 240 models in the ensemble is unique, defined by their parameter values. The initial ensemble of models were generated using a Monte Carlo approach to choose parameter values. As such, we only prescribed that the magma reservoir as a spheroidal geometry, but allowed the EnKF to determine best fit parameters for the ellipsoid shape (size, prolate vs. oblate) and its location (see Table S3 for parameter initial values). During each EnKF analysis step the parameter values for all the models are updated to nudge the ensemble towards a better fit with the observations (see Fig. S2 for details of the EnKF workflow) and over time they converge. Variation in the spread of the model parameters allows for an evaluation of the statistical probability of a particular model state as well as an indication of the EnKF performance. For example, a divergence in the ensemble results indicated by a sudden expansion of the parameter space might suggest that the EnKF is having trouble fitting the observations (12).

Five months prior to the June 26, 2018 eruption of Sierra Negra, we completed an EnKF analysis to track the volcano's stress evolution that turned out to successfully forecast the timing of the subsequent eruption. Because the initial forecast was conducted as a test using a simple elastic rheology and did not assimilate InSAR data before 2014 or after January 2018, we also conducted retroactive forecasts (which we refer to as "hindcasts") to evaluate our findings. The following section details the results of four EnKF numerical experiments which are evaluated on their ability to track the stability of the Sierra Negra magma system through time (Fig. 2; Table S3): 1) the pre-eruption forecast that assimilated ground deformation observations from descending InSAR tracks into an elastic FEM model with a

constant Young's modulus, which was conducted prior to the 2018 eruption; 2) a post-eruption "hindcast" that assimilated all pre-eruption descending InSAR observations into an elastic FEM model with a constant Young's modulus, "nTd"; 3) a post-eruption hindcast that assimilated descending InSAR observations into an elastic FEM model with a temperature-dependent Young's modulus, "Td"; and 4) a post-eruption hindcast that assimilated both ascending and descending InSAR observations into an elastic FEM model with a temperature-dependent Young's modulus, "Tot". The hindcasts with only descending InSAR data are included to provide direct comparisons with the forecast. The full hindcast, "Tot", is the most complete evaluation of the InSAR timeseries data.

## Pre-eruption Forecast

In the fall of 2017, Sierra Negra was chosen as a target for testing near real time data assimilation using the EnKF due to its extensive, ongoing deformation signal observed by the Sentinel-1 InSAR satellite. Although GNSS data are also available for most of the pre-eruption deformation cycle (20), our efforts focus on InSAR data assimilation because the ability to evaluate volcanic activity using satellite data in remote locations where ground-based observations are unavailable is critical for assessing hazards at many volcanoes (5). Additionally, InSAR data provide good spatial constraints reducing non-uniqueness in the model fit, and the lower temporal resolution is less computationally expensive. An important consideration when using data assimilation techniques, such as the EnKF, is that each time step involves significant processing time. Future efforts will incorporate GNSS into the deformation timeseries data analysis as the EnKF technique is further developed and computational efficiency is improved.

 The pre-eruption forecast made in January 2018 utilized a timeseries of InSAR line-of-sight (LOS) displacement calculated from 69 descending acquisition observations (03-07-2015 to 01-26-2018) from the Sentinel-1 satellite. We did not include InSAR data available between 2005-2014, because this initial experiment with EnKF data assimilation was tailored to using Sentinel-1 InSAR data (only available after December 2014). Of particular interest was how the deformation source geometry varied through time, because rapid changes in source geometry and magma input may impact its stability and potential for eruption. However, after an initial spin up period (~10 timesteps) as the ensemble stabilized, the geometry and location of the model reservoir converged and remained relatively constant throughout the remainder of the data assimilation (Fig. 2C-J). Pressure increase was estimated along the boundary of the reservoir (Fig. 2G). Note that, because the EnKF begins with the first InSAR observation in 2015, the full magnitude of pressure accumulated after the 2005 eruption was not tracked, but rather the change in pressure between 2015-2018 was evaluated.

After incorporating the January 26, 2018 InSAR observations, the conditions for failure around the magma reservoir were evaluated to determine the stability of the system (Fig. 3). Andersonian fault orientations were calculated from the modeled stress state in the regions of predicted Mohr-Coulomb failure (using a value of C = 10 MPa for cohesion, following previous analyses of the 2005 eruption (10)) to investigate potential faulting (9, 26). In the mean model from the EnKF ensemble,

some elements near the southern edge of the magma reservoir exhibited tensile stresses > 1 MPa, areas of Mohr-Coulomb failure were observed in the overlying roof, and pressure change in the magma reservoir was ~8 MPa (Figs. 2G, 3A).

The calculated tensile stresses, pressure, and shear failure on January 26, 2018, five months prior to the eruption, were clearly not significant enough to an drive eruption. A year-long forecast was produced by propagating the mean parameter values (and rates of change) from the EnKF ensemble forward through time to evaluate the stability of the system if it were to stay on this same trajectory. Because the pressure evolution was prescribed, the forecast model estimated magma system failure by investigating Mohr-Coulomb failure in the host rock and tensile failure along the magma reservoir boundary. As the model forecast progressed, calculated stress and failure accumulate in the roof above the magma reservoir and became more widespread (Fig. 3B and C). The forecast model produced in January 2018 indicated tensile failure at the magma reservoir and through-going Mohr-Coulomb failure (i.e., continuous shear failure from the surface of the model to the boundary of the pressure source) were likely to occur between June 25, 2018 and July 5, 2018, (Fig. 3C). The 2018 forecast for Sierra Negra was presented in March 2018 at the UNAVCO Science Workshop as a rolling 10-day forecast. The forecast tracked the evolution of failure through 2018 and flagged the period of June 26 – July 5, 2018 as a potential time period for magma system failure (leading to eruption) due to through-going Mohr-Coulomb failure (27).

Several caveats were discussed at the UNAVCO 2018 workshop including the lack of a temperature-dependent rheology in the forecast, the assumption of the failure criteria and host rock strength (e.g., cohesion and tensile strength), the lack of the consideration of the full stress evolution following the 2005 eruption (i.e., what was the initial stress state in early 2015?), and the assumption of the magma system maintaining its January 2018 trajectory going forward. Because our initial forecast for Sierra Negra was conducted as a test for the presentation at the March 2018 UNAVCO Science Workshop, we did not update the forecast in the months leading up to the June 26<sup>th</sup> eruption. Additionally, we had not yet fully tested the temperature-dependent rheology FEM in the EnKF, so that is why it was not included in the initial forecast. Finally, we had only used preliminary InSAR data in the forecast from descending observations for computational expediency. Given these many caveats, additional numerical experiments are necessary to evaluate the successful outcome of the forecast.

## Post-eruption Hindcasts

The Sierra Negra EnKF hindcasts (retroactive forecasts) utilize a timeseries of InSAR line-of-sight (LOS) displacement calculated from 98 descending acquisitions (Track 128, 12-13-2014 to 06-19-2018) and 42 ascending acquisitions (Track 106, 11-19-2016 to 06-18-2018) from the Sentinel-1 satellite (Supplemental Fig. S5). At each time step between InSAR scenes the 240-member ensemble of three-dimensional FEM models were calculated by COMSOL Multiphysics. As previous modeling efforts indicate that a temperature-dependent rheology may be necessary for Sierra Negra (10), two of the hindcasts included an elastic rheology with a temperature-dependent Young's modulus. One temperature-dependent

247

198

199

200

201 202

203

204

205

206

207 208

209

210

211

212

213

214

215 216

217 218

219

220

221

222 223

224

225

226

227

228 229

230

231

232

233

234

235

236 237

238 239

240

241

242

243 244

245

248 hindcast (Td) used only descending InSAR observations for direct comparison with 249 the pre-eruption forecast, while the other assimilated both ascending and 250 descending observations into the temperature-dependent model (Tot). A non-251 temperature dependent hindcast (nTd) was provided for comparison. Since previous 252 studies indicate that the viscous component of the rheology may be negligible for 253 the timescale of the evaluated unrest period (28), the EnKF has been developed to 254 work with elastic rather than viscoelastic constitutive models in the finite element 255 analysis.

There is generally very close agreement between the forecast and hindcasts as to the location and geometry of the pressure source (Fig. 2). Small differences are likely due to the improved InSAR timeseries data produced for the hindcast and improvements to the EnKF method. The largest differences between the four experiments appear in the estimation of pressure change (Fig. 2G), which varies from ~9 MPa at the time of the eruption for the total hindcast (Tot, green dots) to 30 MPa of pressure change in the temperature-dependent hindcast (Td, blue dots). The increasing model covariance in the Td model, as observed by the expanding 2-sigma error bars, is due to a test of the EnKF for the Td model in which the parameters are normalized such that overpressure and radius have the same magnitude. Since parameter scaling did not improve the EnKF performance, and in fact decreased its performance, it was not used in subsequent experiments. The spread in the ensemble from the Tot hindcast, which uses both ascending and descending InSAR observations, remains low indicating a higher EnKF confidence.

An advantage of the ensemble modeling approach is that the percentage of models in failure can be tracked for a statistical evaluation of the potential eruption triggering mechanisms (Fig. 4). We utilize the total hindcast (Tot) to evaluate system evolution in the lead up to the eruption since it assimilated the most complete InSAR data set and resulted in the best EnKF performance. The percentage of ensemble members experiencing Mohr-Coulomb failure in the host rock (Fig. 4A) and tensile failure along the reservoir boundary (Fig. 4B) are tracked at each data assimilation time step. As the cohesion (C) and tensile strength (Tc) of the rock are uncertain, several values are evaluated for each. In late 2017, a rise in the percent of models in the EnKF ensemble experiencing Mohr-Coulomb failure, using a cohesion value of C = 20 MPa, coincides with an increase in the recorded seismicity in the Sierra Negra Caldera (29). By the end of 2017. > 60% of the models in the EnKF ensemble experienced Mohr-Coulomb failure (C = 20 MPa) in the roof above the reservoir. However, during this same period, < 40% of the models in the EnKF ensemble experienced tensile failure along the reservoir boundary (Fig. 4B,  $Tc \le 1$  MPa), and the mean ensemble model calculates no tensile failure.

In the lead up to the June  $26^{th}$  eruption, a greater percentage of models exhibit reservoir tensile failure (Fig. 4B) as the estimated change in pressure increases to 10 MPa (Fig. 2G). In the time steps prior to the eruption, > 80% of models indicate tensile failure focused along the southern, shallower edge of the magma reservoir (Fig. 4D, Tc = 5 MPa), opposite of where most of the fissures erupted along the northern rim and flanks of the caldera (Fig. 1B). Curiously, the reservoir beneath the northern region of the caldera does not appear to be in tensile failure at the final time step in any of the ensemble models (Tc = 1 MPa). Rather, the northern side of

256257

258

259

260

261

262

263

264

265

266267

268269

270

271

272273

274

275

276277

278

279

280

281

282

283

284 285

286

287

288

289

290291

292

293

294

295

296

the magma system is calculated to have remained in compression leading up to the eruption. Therefore an additional catalyst or system wide stress change was apparently required to promote tensile failure and dike initiation to the north.

Andersonian fault orientations are calculated from the modeled stress state in the regions of predicted Mohr-Coulomb failure (here using a cohesion value of C = 10 MPa, to be consistent with the pre-eruption forecast) to investigate potential faulting sources (Fig. 4C and 4D) (9, 26). By late 2017, significant regions of the shallow roof experience shear failure (Fig. 4C). Normal faulting is predicted directly above the pressure source, with reverse faulting calculated above the outer edges. As the model progressed through 2018, the area of failure became more extensive and by June  $26^{th}$  shear failure was calculated to be through-going in the entire southern region of the system (C = 10 MPa).

Ten hours prior to the June 26th eruption, a Mw 5.4 earthquake struck on the southern portion of the Sierra Negra caldera along a north-dipping reverse fault coincident with the region of extensive Mohr-Coulomb failure calculated by the EnKF hindcast (20, 22). The calculated moment tensor source of the earthquake is in agreement with model predicted fault orientations (Fig. 4D). Based on previous calculations indicating that the 2005 eruption of Sierra Negra may have been triggered by a Mw 5.5 earthquake in a similar location (10), we investigated the stress change due to the June 26th earthquake utilizing the USGS Coulomb 3.4 software (30, 31). Coulomb static stress change indicates that the region to the north of the earthquake may have experienced significant unclamping in response to the event (Fig. 5). Since the magma reservoir was near tensile failure, but had not yet ruptured, the trapdoor faulting event almost certainly triggered eruption. Additionally, compressional stress is estimated to increase directly above the reservoir, promoting dike deflection and fissure opening to the north of the caldera (Fig. 5A). The trapdoor earthquake appears to have buffered the model-predicted tensile failure along the south edge of the reservoir, allowing the coulomb static stress change to induced failure on the northern edge instead.

#### Discussion

#### Seismic precursors and earthquake triggering

A key feature of the Sierra Negra magma system is the interplay between the caldera trapdoor fault system and the magma chamber (3, 19, 20, 32). In the total hindcast (Tot) of the Sierra Negra system, overpressure and tensile failure remain insignificant while shear failure becomes widespread in the surrounding crust. Given the timing and spatial location of the eruption in context with the Mw 5.4 earthquake, and the similarity to the sequence in 2005, it is likely (almost certain) that the two are intrinsically linked. If the Mw 5.4 faulting event had not occurred, the EnKF indicates that the magma system was tending towards increasing tensile stress along the northern and southern edges of the reservoir (Fig. 3C and 3D) and an eruption triggered through dike initiation was increasingly likely. However, it appears that the timing was expedited by the trapdoor faulting event.

The initial stress state

A critical issue in volcano forecasting is determining the initial stress state of the system. Unfortunately, capturing a full eruption cycle from an initial ambient stress

346347

298

299

300

301 302

303

304

305

306

307 308

309

310

311

312313

314

315

316

317

318

319320

321 322

323

324325

326327

328329330

331332

333334

335

336

337

338339

340

341

342

state through to eruption is a difficult prospect given that few systems have long term monitoring spanning multiple eruptions, and a system may not reach a fully relaxed stress state after an eruption prior to continued unrest. In the case of Sierra Negra, the model forecasts and hindcasts were initiated when Sentinel-1 InSAR data became available in 2014, thus neglecting the prior decade-long stress evolution which followed its 2005 eruption. During this time period, upwards of 4 meters of uplift was recorded by GNSS (20), which is absent in the Sentinel-1 InSAR only approach. Capturing a full eruption cycle with the complete magnitude of deformation is an important next step in the development and testing of the EnKF method.

Fortunately, in the absence of a full eruption cycle, the EnKF can be tuned to capture failure and stress change as the system evolves. The rheology of the host rock assumed in the model can be adjusted in the absence of information on the pre-existing stress state. In the case of a protracted unrest period, a weaker crust is necessary to inhibit failure and eruption of the system. In that sense, the weakened Young's modulus provided by a temperature-dependent rheology was key for the Sierra Negra hindcasts. Additionally, the chosen failure criteria are equally important. As such, the failure criteria used in this investigation likely reflect a minimum rather than the true failure envelope for the system. Were the entire deformation period tracked, a higher tensile strength and cohesion would have been necessary to match the EnKF forecasts with the observations of seismicity and the timing of eruption at Sierra Negra. Future rock deformation experiments are necessary to constrain parameters such as cohesion and tensile strength. Until then, tracking a variety of failure envelopes is required.

## Pressure evolution in the lead up to the eruption

A critical or maximum overpressure is often cited as a means for triggering an eruption through the initiation and propagation of a dike (33). Our approach does not preclude pressure as an eruption catalyst, but rather postulates that pressure build up in a magma system is the means for promoting tensile and/or shear failure, which in turn triggers magma migration that may lead to eruption. However, volume change without significant overpressurization will result in the same strain accumulation in the host rock leading to tensile and/or shear failure. Unfortunately, it is difficult to differentiate between the two (volume vs. pressure) because of inherent non-uniqueness of the modeling approach (34). The key, however, is estimating the stress in the host rock to determine whether the areas surrounding a magma system are near to failure.

The pressure state of the magma system may be linked to the intensity of the subsequent eruption. As such, a key observation for constraining the pre-eruption magma reservoirs pressure state might be the magnitude of the eruption. In the case of the 2018 eruption of Sierra Negra, pressure within the reservoir was significant enough to drive diking and produce multiple fissure openings to the north and west of the caldera (22). The apparently modest change in pressure estimated by the EnKF (~ 10 MPa), may be an appropriate order of magnitude and adequate to drive the 2018 eruption. However, significantly more research must be done to quantify pressure variations within a magma system to better understand the role of magma pressure in triggering dike initiation and eruptions. Until pressure variations can be better constrained, models of stress change and failure in the surrounding host rock,

which can be linked more directly to observations of seismicity and deformation, provide an important approach for investigating eruption triggering mechanisms.

399400401

402 403

404 405

406

407 408

409

410 411

412

413 414

415

416

398

Forecasting the June 26, 2018 eruption

In many ways, the forecast provided by the EnKF five months ahead of the June 26<sup>th</sup> earthquake and eruption (27), can be chalked up to "accidental good fortune". The forecast was based on rough estimates of physical properties, required the system to remain on the inflation trajectory determined on January 26, 2018, and relied on an assumption for what constitutes system failure. Specifically, system failure was flagged when Mohr-Coulomb failure calculated in the host rock was through-going, from the surface of the model to the magma chamber boundary (9), using a cohesion of 10 MPa which appeared to work well for the 2005 eruption of Sierra Negra (10), and a constant Young's Modulus. It is unclear whether the through-going failure flagged by the EnKF forecast was forecasting the potential of the June 26<sup>th</sup> earthquake or the eruption. We posit that the more important outcome is the success of the EnKF to quantify deformation, stress, and failure as indicators to track the evolution of the system. The apparently successful eruption forecast of Sierra Negra illustrates the potential for evaluating magma system stress evolution in real-time using the EnKF approach. This framework has transformative implications for forecasting volcanic unrest with higher fidelity in the future, which is particularly important in densely populated areas near active volcanoes.

417 418 419

# **Materials and Methods**

421 422 423

424 425

426 427

428 429

430

431

432

420

Finite Element Method Approach

Our numerical approach utilizes previously developed and benchmarked, thermomechanical finite element method (FEM) models (9). COMSOL

Multiphysics is used to calculate the stress, strain, and temperature variations due to a pressurized magma chamber in a 3D linear elastic space (Fig. 2A). A free surface is assumed at the top of the model space, roller boundary conditions are applied on the side and base of the model. The magma chamber is represented by a pressurized ellipsoid that is free to move in space, and rotate in strike and dip (Fig. 2B). Model parameters and variables are provided in Supplemental Tables S1 and S2, respectively. The geometrical and spatial parameters describing the magma reservoir are varied by the EnKF analysis described below.

433 434 435

436

437

438

The mechanical behavior of the model is governed by the quasi-static conservation of momentum:

$$\Box \, \Box \boldsymbol{\sigma} + \mathbf{b} = 0,$$
(1)

where  $\sigma$  is the Cauchy stress tensor and  ${\bf b}$  is the body force density vector.

439 440 441

442

The presented COMSOL models utilize the COMSOL Floating Network License (FNL) for cluster computing, the Heat Transfer Module, and Structure Mechanics Module. EnKF results are plotted using Python and the COMSOL MATLAB LiveLink is used for model visualization.

443444445

446

Thermal model for temperature-dependent hindcasts (Td and Tot)

A new steady state thermal structure is calculated for each model in the EnKF ensemble for each time step (Supplemental Fig. S1A). The steady-state thermal structure is solved numerically by COMSOL from the steady-state heat conduction equation:

$$\nabla \cdot (k\nabla T) = -Q,$$
(2)

where k is the thermal conductivity, T is temperature, and Q is the crustal volumetric heat production, assumed to be zero. A magma temperature is of  $1100^{\circ}$ C is assumed along the reservoir boundary. A background geotherm of  $30^{\circ}$ C/km is assumed. Although volcanic systems are transient and unlikely to reach a steady state thermal equilibrium, this provides an end-member starting point. A non-temperature dependent, elastic hindcast is provided for comparison.

We are particularly interested in the impact of the thermal structure on the elastic properties of the host rock and the resultant model predictions. As such, we have incorporated a temperature and depth-dependent Young's modulus (35):

$$E_{Td} = E_b - E_b \left( \exp\left(\frac{T + zT_{geo}}{T_m}\right) - 1 \right) * 0.5,$$
(3)

where a far-field, depth-dependent Young's modulus ( $E_b = -6.9z^2 - 1.3 \times 10^6z + 5 \times 10^{10} \ Pa$ ) is assumed in the brittle region of the model space (36),  $T_m$  is the magma reservoir temperature, and  $T_{geo}$  is the geothermal gradient (Supplemental Fig. S1B). Equation 3 provides a smooth transition between the brittle and ductile Young's modulus to minimize computational issues and mimic nature, which likely has a transition in material properties rather than a sharp boundary.

#### Failure estimation

Failure in the host rock surrounding a reservoir is critically important for determining the stability of the system and potential for eruption. We use a combination of two approaches to predict magma chamber stability. First, we investigate faulting and failure in the brittle portions of the model space using a Mohr-Coulomb failure criterion:

$$\tau = C + f\sigma_n,$$
(4)

where  $\tau$  is the shear stress at failure, C is cohesion, f is the internal friction coefficient, and  $\sigma_n$  is the mean stress normal to the failure plane (37). Second, we investigate the evolution of tensile stresses,  $\sigma_{ts}$ , which are defined as the least compressive stress along the magma chamber boundary. In application, as a magma system grows and inflates, the expansion results in flexure and uplift of the overlying roof, promoting faulting and brittle failure. The Andersonian fault orientations of the model elements in the predicted region of failure are tracked to evaluate the fault types predicted during magma system evolution (9, 26, 38, 39). Simultaneously, tensile stresses along the chamber boundary can result in Mode-I failure and dike initiation (26).

495496

497

498

499

500

501

502 503

504

505

506

507

508

509

510

511

512513

514

515

516

517518

519520

521

522

523

524

525

Ensemble Kalman Filter (EnKF)

Model-data fusion strategies are critical for producing model forecasts of complex system behavior. We have adapted the EnKF (12), an ensemble-based Markov chain Monte Carlo (MCMC), sequential data assimilation approach, to assimilate large geospatial data into multiphysics volcano FEMs (13, 14). The ensemble-based EnKF can be applied with FEMs and circumvents the linearity and computational issues inherent to other Kalman filtering approaches (13). Additionally, the EnKF is highly parallelizable. The workflow (Supplemental Fig. S2) has been adapted for High Performance Computing (HPC) utilizing a handshake between Python and COMSOL Multiphysics. The HPC EnKF approach is highly scalable and individual FEM models are distributed across compute nodes for swift, simultaneous calculation at each data assimilation time step. In practice, every time a new InSAR observation becomes available from Sierra Negra, the new data are assimilated to provide parameter updates for the models in the EnKF ensemble. The updated models are then propagated forward in time to provide updated forecasts of the volcanic system state. As more data, D, become available, the model errors are reduced and the forecasts are refined. Measurements and models are combined in the EnKF analysis step to provide the analysis ensemble, Aa:

$$\mathbf{A}^{\mathbf{a}} = \mathbf{A} + \mathbf{X} \mathbf{H}^{\mathsf{T}} (\mathbf{H} \mathbf{X} \mathbf{H}^{\mathsf{T}} + \mathbf{C}_{\mathsf{d}})^{-1} (\mathbf{D} - \mathbf{H} \mathbf{A}),$$
(5)

where X is the ensemble covariance matrix,  $C_d$  is the measurement covariance matrix, and H is the model operator matrix (12-14).

For the Sierra Negra implementation, 240 COMSOL FEM models are calculated at each timestep on a cutting-edge, high-performance computing system at the National Center for Supercomputing Applications. A COMSOL Cluster Sweep is used to distribute the parameter values estimated by the EnKF analysis step to produce 240 models, which are distributed across compute nodes and CPUs. Due to the inherent overhead of the COMSOL software, 240 models provide an optimal speed up. Additionally, previous testing has indicated that as few as 100 ensembles provide a sufficient convergence for the EnKF approach (12). Future EnKF implantations with open source modeling approaches will allow for more flexibility.

526527528

529

530

531532

533534

535

Coulomb static stress transfer

To investigate the static stress change resulting from the 26 June 2018  $M_{\rm w}$  5.4 earthquake we utilize the USGS Coulomb 3.4 Coulomb static stress software (30, 31). The Coulomb stress change is defined as:

$$\Delta CFF = \Delta \tau + \mu_f \Delta \sigma_n,$$
(6)

where  $\Delta \tau$  is the change in shear stress (positive in the slip direction),  $\mu_f$  is the apparent friction coefficient, and  $\Delta \sigma_n$  is the change in normal stress (positive indicates unclamping).

536537538

539

540

541

The fault plane solution for the 26 June 2018 was determined by seismic wave form and InSAR analysis (20). The Scalar Moment is estimated as 1.73e24 dyne cm, with a strike of 248°, dip of 65°, and rake of 90°. The location is thought to be along the southern trapdoor fault evidenced by a sinuous ridge in the Sierra Negra

caldera. The location is further corroborated by ground observations collected after the event (20). We calculate the Coulomb stress change for receiver faults oriented with a strike of 105°, dip of 65°, the complementary orientation of faults on the opposite side of the Sierra Negra caldera.

545546547

548

549

550

551552

553

554

555

556

557

558

559560

561

542

543

544

## InSAR Data Processing

To measure the surface deformation over the Sierra Negra caldera, using MintPy software (https://github.com/yunjunz/MintPy) we apply the small baseline InSAR time series analysis approach (40) to the Sentinel-1 descending track 128 subswath 1 dataset from 13 December 2014 to 26 January 2018 (69 acquisitions) and from 13 December 2014 to 16 June 2018 (98 descending and 42 ascending acquisitions) for the hindcasts. We generated a network of interferograms with five sequential connections for each acquisition using the stack Sentinel processor (41) within JPL/Caltech's ISCE software (42). We multilook each interferogram by 15 and 5 looks in range and azimuth direction respectively, filter using a Goldstein filter with a strength of 0.2. We remove the topographic phase component using SRTM DEM (SRTMGL1, ~30m, 1 arc second with void-filled; (43)). The interferograms are phase-unwrapped using the minimum cost flow method (44). We correct the displacement time-series for the stratified tropospheric delay using the ERA-Interim weather re-analysis dataset (45), topographic residual (46). Reliable pixels are selected using a temporal coherence threshold of 0.7 (47).

562563564

565

566

It is computationally prohibitive to assimilate data from the entire InSAR database. As such, a QuadTree algorithm based on root-mean-square-error of the displacement values is applied to reduce the number of samples for each epoch of InSAR data from ~150,000 to ~500.

567568569

#### References

570571572

573

- 1. E. National Academies of Sciences, and Medicine, *Volcanic Eruptions and their Repose, Unrest, Precursors, and Timing*. E. National Academies of Sciences, and Medicine, Ed., (National Academies Press, Washington D. C., 2017).
- 575 2. K. Mogi, Relations of the eruptions of various volcanoes and the deformations of the ground surface around them. *Bull. Earthq. Res. Inst., University of Tokyo* **36**, 577 99-134 (1958).
- 578 3. F. Amelung, S. Jonsson, H. Zebker, P. Segall, Widespread uplift and 'trapdoor' 579 faulting on Galapagos volcanoes observed with radar interferometry. *Nature* **407**, 580 993-996 (2000).
- J. Biggs, M. E. Pritchard, Global Volcano Monitoring: What Does It Mean When Volcanoes Deform? *Elements* **13**, 17-22 (2017).
- 583 5. J. Biggs *et al.*, Global link between deformation and volcanic eruption quantified by satellite imagery. *Nature Communications* **5**, (2014).
- 585 6. R. White, W. McCausland, Volcano-tectonic earthquakes: A new tool for estimating intrusive volumes and forecasting eruptions. *Journal of Volcanology and Geothermal Research* **309**, 139-155 (2016).
- 7. C. E. Cameron *et al.*, Alaska Volcano Observatory Alert and Forecasting Timeliness: 1989-2017. *Frontiers in Earth Science* **6**, (2018).

- 590 8. E. Chaussard, F. Amelung, Y. Aoki, Characterization of open and closed volcanic 591 systems in Indonesia and Mexico using InSAR time series. Journal of Geophysical 592 Research-Solid Earth 118, 3957-3969 (2013).
- 593 9. P. M. Gregg, S. L. de Silva, E. B. Grosfils, J. P. Parmigiani, Catastrophic caldera-594 forming eruptions: Thermomechanics and implications for eruption triggering and 595 maximum caldera dimensions on Earth. Journal of Volcanology and Geothermal 596 Research 241-242, 1-12 (2012).
- 597 10. P. M. Gregg et al., Stress Triggering of the 2005 eruption of Sierra Negra volcano, 598 Galápagos. Geophysical Research Letters, (2018).
- 599 A. Carrassi, M. Bocquet, L. Bertino, G. Evensen, Data assimilation in the 11. 600 geosciences: An overview of methods, issues, and perspectives. Wiley Interdiscip. 601 Rev.-Clim. Chang. 9, (2018).
- 602 G. Evensen, Data Assimilation: The Ensemble Kalman Filter, Second Edition. 12. 603 (Springer, Heidelberg, 2009).
- P. M. Gregg, J. C. Pettijohn, A multi-data stream assimilation framework for the 604 13. assessment of volcanic unrest. Journal of Volcanology and Geothermal Research 605 606 **309**, 63-77 (2016).
- Y. Zhan, P. M. Gregg, Data assimilation strategies for volcano geodesy. *Journal of* 607 14. 608 *Volcanology and Geothermal Research*, (2017).
- 609 15. M. G. Bato, V. Pinel, Y. Yan, Assimilation of Deformation Data for Eruption 610 Forecasting: Potentiality Assessment Based on Synthetic Cases. Frontiers in Earth 611 Science 5, (2017).
- 612 J. A. Albright, P. M. Gregg, Z. Luz, J. T. Freymueller, Hindcasting Magma 16. 613 Reservoir Stability Preceding the 2008 Eruption of Okmok, Alaska. Geophysical 614 Research Letters 46, 8801-8808 (2019).
- 615 17. R. W. Reynolds, D. J. Geist, Petrology of lavas from Sierra Negra volcano, Isabela Island, Galapagos archipelago. Journal of Geophysical Research-Solid Earth 100, 616 617 24537-24553 (1995).
- D. J. Geist et al., The 2005 eruption of Sierra Negra volcano, Galapagos, Ecuador. 618 18. 619 Bulletin of Volcanology **70**, 655-673 (2008).
- 620 W. W. Chadwick, Jr. et al., A volcano bursting at the seams: Inflation, faulting, and 19. 621 eruption at Sierra Negra volcano, Galapagos. Geology 34, 1025-1028 (2006).
- 622 20. A. F. Bell et al., Caldera resurgence during the 2018 eruption of Sierra Negra 623 volcano, Galápagos Islands, Nature Communications 12, (2021).
- 624 21. A. F. Bell, S. Hernandez, P. C. La Femina, M. C. Ruiz, Uplift and Seismicity 625 Driven by Magmatic Inflation at Sierra Negra Volcano, Galapagos Islands. Journal 626 of Geophysical Research-Solid Earth 126, 18 (2021).
- 627 22. F. Vasconez et al., The different characteristics of the recent eruptions of 628 Fernandina and Sierra Negra volcanoes (Galápagos, Ecuador). Volcanica 1, 127-629 133 (2018).
- S. Jonsson, Stress interaction between magma accumulation and trapdoor faulting 630 23. 631 on Sierra Negra volcano, Galapagos. *Tectonophysics* **471**, 36-44 (2009).
- S. Jonsson, H. Zebker, F. Amelung, On trapdoor faulting at Sierra Negra volcano, 632 24. 633 Galapagos. Journal of Volcanology and Geothermal Research 144, 59-71 (2005).
- 634 25. S.-H. Yun, H. A. Zebker, P. Segall, A. Hooper, M. Poland, Eruption at Sierra Negra 635 volcano unveiled by InSAR observations. Eos Trans. AGU 87, Abstract G52A-01 636 (2006).
- 637 26. E. B. Grosfils, Magma reservoir failure on the terrestrial planets: Assessing the 638 importance of gravitational loading in simple elastic models. *Journal of* 639 Volcanology and Geothermal Research 166, 47-75 (2007).

- 640 27. P. M. Gregg et al., Imaging volcano deformation sources through geodetic data 641 assimilation. UNAVCO Science Workshop Abstracts, (2018).
- 642 Y. Zhan, P. M. Gregg, How accurately can we model magma reservoir failure with 28. 643 uncertainties in host-rock rheology? J. Geophys. Res., (2019).
- 644 29. F. Vasconez et al., The different characteristics of the recent eruptions of 645 Fernandina and Sierra Negra volcanoes (Galápagos, Ecuador. Volcanica 1, 127-133 646
- 647 30. J. Lin, R. S. Stein, Stress triggering in thrust and subduction earthquakes and stress interaction between the southern San Andreas and nearby thrust and strike-slip 648 faults. Journal of Geophysical Research-Solid Earth 109, (2004). 649
- 650 31. S. Toda, R. S. Stein, K. Richards-Dinger, S. B. Bozkurt, Forecasting the evolution 651 of seismicity in southern California: Animations built on earthquake stress transfer. 652 Journal of Geophysical Research-Solid Earth 110, (2005).
- 653 32. A. F. Bell et al., Dynamic earthquake triggering response tracks evolving unrest at 654 Sierra Negra volcano, Galapagos Islands. Sci. Adv. 7, 9 (2021).
- A. M. Rubin, Propagation of magma-filled cracks. Annu. Rev. Earth Planet. Sci. 23, 655 33. 656 287-336 (1995).
- J. Albright, P. M. Gregg, paper presented at the IGARSS 2020 2020 IEEE 657 34. 658 International Geoscience and Remote Sensing Symposium, Waikoloa, HI, USA, 659 2020.
- 660 R. Smith, P. R. Sammonds, C. R. J. Kilburn, Fracturing of volcanic systems: 35. 661 Experimental insights into pre-eruptive conditions. Earth and Planetary Science Letters 280, 211-219 (2009). 662
- Y. Zhan, P. M. Gregg, H. Le Mevel, C. A. Miller, C. Cardona, Integrating 663 36. Reservoir Dynamics, Crustal Stress, and Geophysical Observations of the Laguna 664 665 del Maule Magmatic System by FEM Models and Data Assimilation. Journal of Geophysical Research-Solid Earth, (2019). 666
- 667 J. F. Labuz, A. Zang, Mohr-Coulomb Failure Criterion. Rock Mech. Rock Eng. 45, 37. 668 975-979 (2012).
- R. W. Simpson, Quantifying Anderson's fault types. J. Geophys. Res 102, 17909-669 38. 17919 (1997). 670
- 671 39. E. B. Grosfils et al., in Volcanism and Tectonism Across the Inner Solar System, T. 672 Platz, M. Massironi, P. Byrne, H. Hiesinger, Eds. (Geological Society, London, 673 Special Publications, 2015), vol. 401, pp. 139-158.
- 674 40. P. Berardino, G. Fornaro, R. Lanari, E. Sansosti, A new algorithm for surface 675 deformation monitoring based on small baseline differential SAR interferograms. 676 *IEEE Transactions on Geoscience and Remote Sensing* **40**, 2375-2383 (2002).
- 41. 677 H. Fattahi, P. Agram, M. Simons, A Network-Based Enhanced Spectral Diversity 678 Approach for TOPS Time-Series Analysis. IEEE Transactions on Geoscience and 679 Remote Sensing 55, 777-786 (2016).
- 680 P. A. Rosen, E. M. Gurrola, G. F. Sacco, H. Zebker, in EUSAR 2012; 9th European 42. 681 Conference on Synthetic Aperture Radar. (VDE, Nuremberg, Germany, 2012).
- 682 43. T. G. Farr et al., The shuttle radar topography mission. Reviews of Geophysics 45, 683 (2007).
- 684 44. C. W. Chen, H. A. Zebker, Two-dimensional phase unwrapping with use of statistical models for cost functions in nonlinear optimization. J. Opt. Soc. Am. A-685 686 Opt. Image Sci. Vis. 18, 338-351 (2001).
- 687 45. R. Jolivet, R. Grandin, C. Lasserre, M. P. Doin, G. Peltzer, Systematic InSAR 688 tropospheric phase delay corrections from global meteorological reanalysis data. 689 Geophysical Research Letters 38, L17311 (2011).

- 46. H. Fattahi, F. Amelung, DEM error correction in InSAR time series. *IEEE Transactions on Geoscience and Remote Sensing* 99, (2013).
  - 47. A. Pepe, R. Lanari, On the extension of the minimum cost flow algorithm for phase unwrapping of multitemporal differential SAR interferograms. *Ieee Transactions on Geoscience and Remote Sensing* **44**, 2374-2383 (2006).

## Acknowledgments

692

693

694

695 696

697 698

699

700 701

702

703

704

705

706

707

708

709

710

711

712

713

714

715

716

717

718

719 720 721

The development of a high-performance computing data assimilation framework for forecasting volcanic unrest is supported by grants from the U.S. National Science Foundation (OCE 1834843, EAR 1752477, EAR 2122745 – Gregg), NASA (13-ESI13-0034 – Amelung and Gregg; 80-NSSC19K-0357 – Gregg), a NASA Earth and Space Science Fellowship (Zhan), and a National Center for Supercomputing Applications Faculty Fellow (Gregg). Geist's work is based upon work supported while serving at the US National Science Foundation. This research is part of the Blue Waters sustained-petascale computing project, which is supported by the National Science Foundation (OCI-0725070 and ACI-1238993) and the state of Illinois. Blue Waters is a joint effort of the University of Illinois at Urbana-Champaign and its National Center for Supercomputing Applications. The authors thank two anonymous reviewers and W. Chadwick who's comments and suggestions greatly enhanced this manuscript. Author Contributions: PMG developed the EnKF approach for volcano forecasting, which YZ enhanced by developing the HPC EnKF. PMG and YZ planned and applied the numerical implementation for Sierra Negra with high performance computing guidance from SK. PMG developed and ran the Coulomb 3.4 models and drafted the manuscript and figures. InSAR data were processed and provided by FA and ZY. DG and PM provided background on the eruptions and the structure of the volcano. All authors discussed the results and commented on the manuscript. **Competing interests:** Authors declare no competing interests. **Data and materials availability:** All data is available in the main text or the supplementary materials.

**Figures and Tables** 

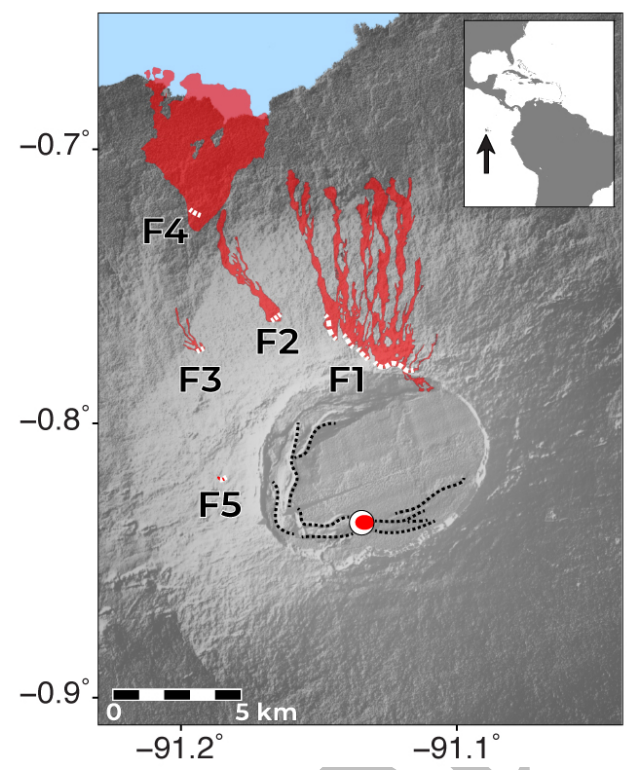


Fig. 1. Sierra Negra's June 26, 2018 Mw 5.4 earthquake and eruption. The eruption commenced on June 26 at 1340 LT from five fissures (white dashed lines, indicated by F1 - F5) with resultant lava flows indicated by red shaded regions (29). Black dashed lines indicate the location of the trapdoor fault system on the southern and southwestern portion of the caldera. Focal mechanism shows the location of the Mw 5.4 earthquake.

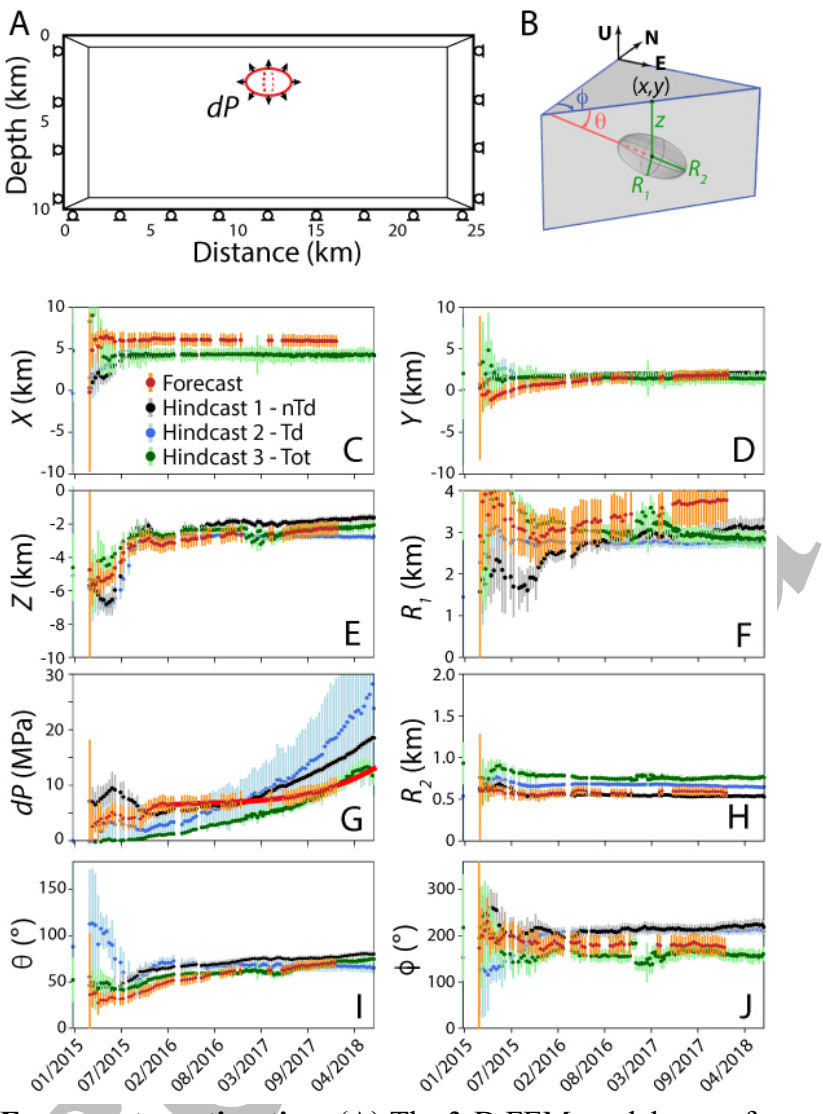


Fig. 2. EnKF parameter estimation. (A) The 3-D FEM model setup for a pressurized reservoir. Full model details are provided in the Supplementary Information. Four EnKF model suites were run to track the evolving Sierra Negra magma system. (B) The ellipsoidal pressure source in the FEM is free to rotate and dip in up-down (U), east-west (E), north-south (N) space. The pre-eruption forecast model utilizes selected Sentinel-1 InSAR data from December 2014 to January 26, 2018 (red dots indicating the ensemble mean, with orange error bars indicating 2sigma standard deviation). Subsequently, three hindcasts were conducted using additional Sentinel-1 InSAR data up to the eruption: a non-Temperature-dependent elastic model that assimilates descending InSAR data only (nTd, black dots with gray error bars, depicting 2-sigma standard deviation), a model with a temperaturedependent Young's Modulus that assimilates descending InSAR data only (Td, blue dots with blue error bars), and a temperature-dependent model which assimilates both ascending and descending InSAR observations (Tot, green dots with green error bars). (C)-(E) Show the predicted spatial parameters, X and Y, and depth, Z. (**F**) and (**H**) provide geometrical constraints,  $R_1$  and  $R_2$ . (**G**) The evolution of magma reservoir pressure, dP. A pressure evolution was produced for the forecast based on the trajectory of the previous two years of deformation (red solid line). (I) The dip of the reservoir,  $\theta$ . (**J**) The strike of the longer  $R_I$  axis of the ellipsoidal reservoir,  $\phi$ .

733

734

735

736

737

738

739

740

741

742

743

744

745

746

747

748

749750

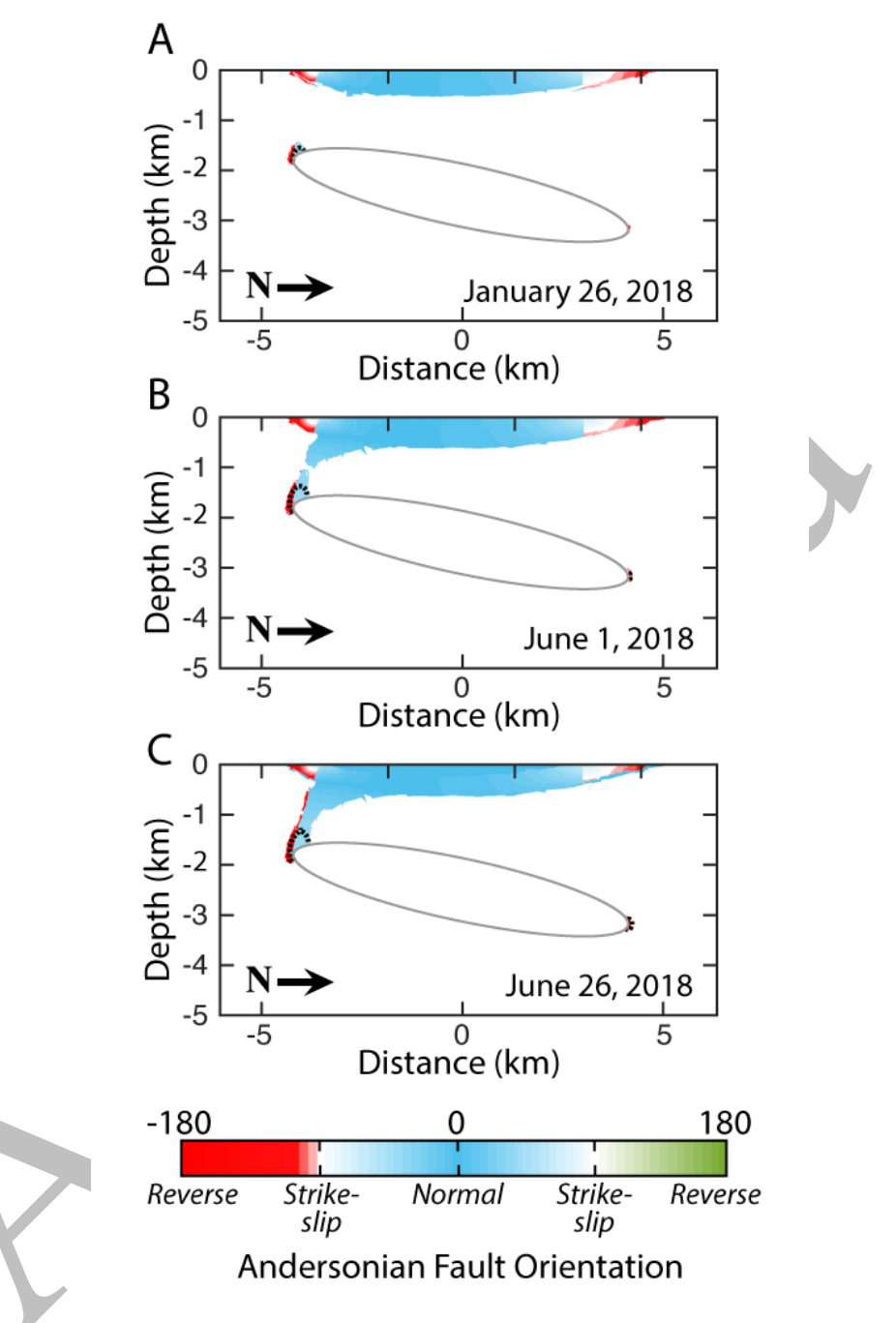


**Fig. 3. Sierra Negra pre-eruption failure forecast.** North-south cross sections are shown through the center of the deformation source calculated by the mean EnKF model (star in Fig. 5B). The mean EnKF model calculated on January 26, 2018 is propagated forward in time following the pressure trajectory determined by the previous 2 years of deformation (Fig. 2G) to provide calculations of the stress state on June 1, 2018 and June 26, 2018. Colors represent calculated Andersonian fault orientations (38) in regions of predicted Mohr-Coulomb failure, assuming a cohesion of C = 10 MPa. Black dashed outlines indicate regions of calculated tensile failure near the reservoir boundary assuming a tensile strength of Tc = 1 MPa.

18 of 20

770

771

772773

774

775776

777

778779

780

781

782 783

784

785

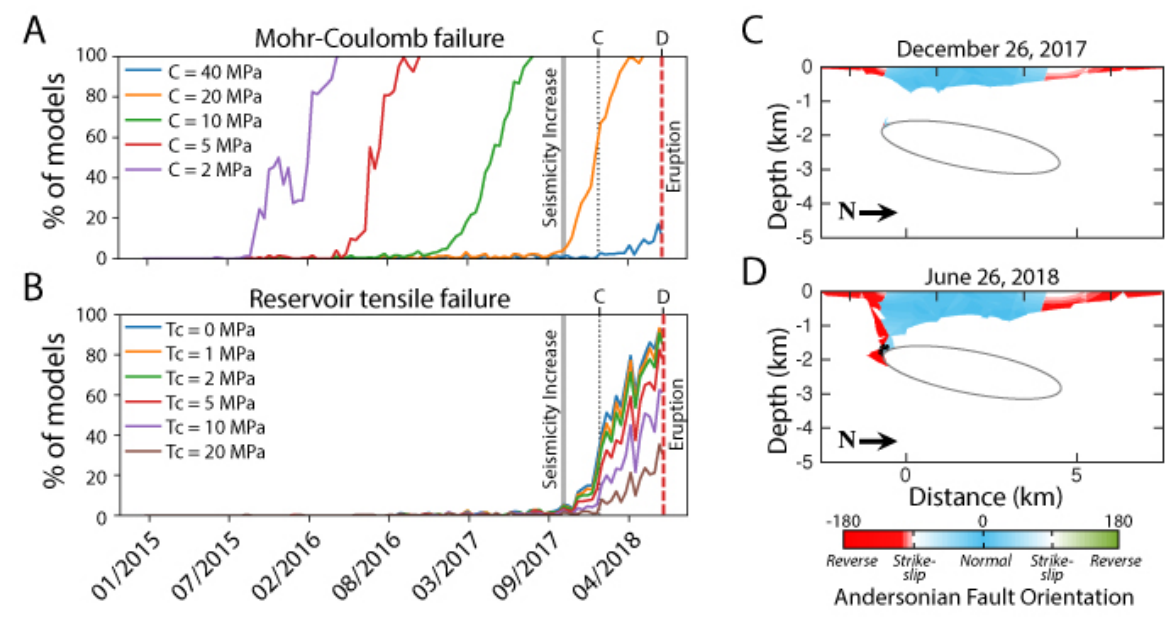
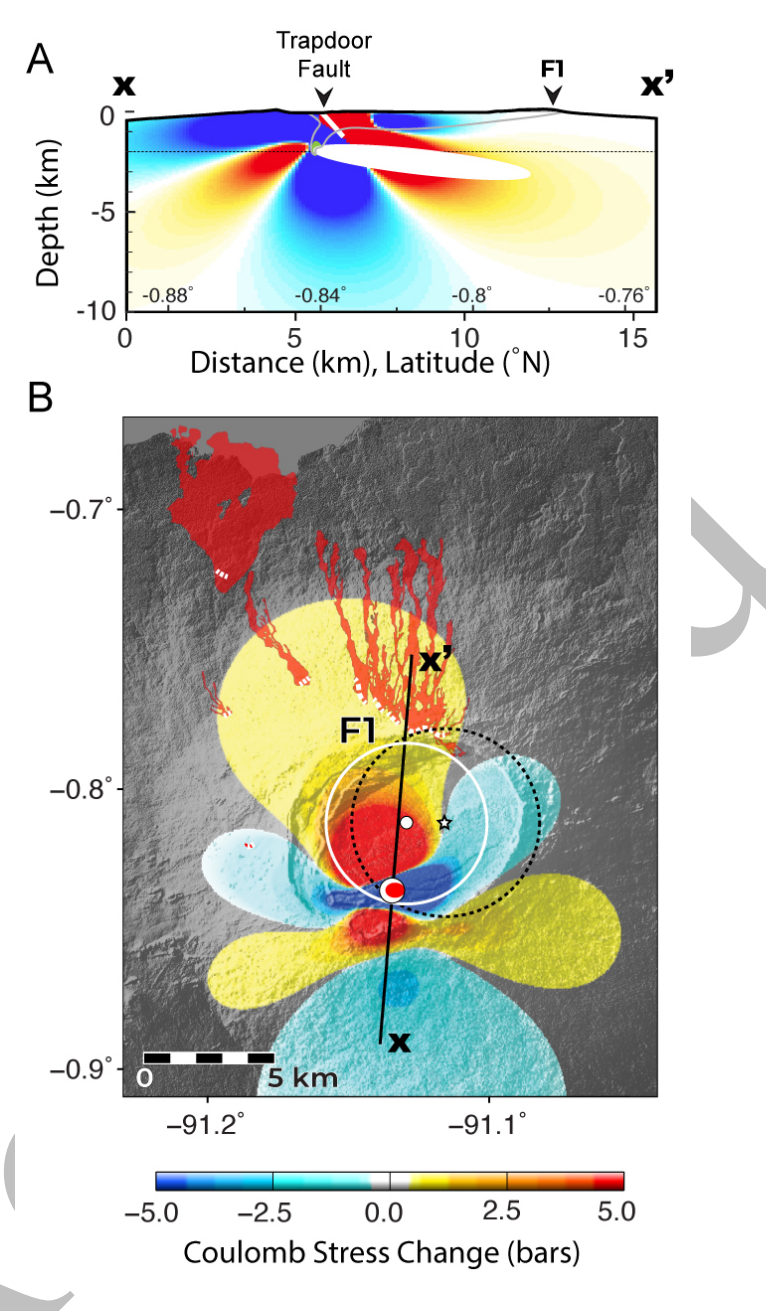


Fig. 4. Failure calculations from the "Tot" Hindcast. (A) The percentage of models in the EnKF ensemble experiencing Mohr-Coulomb failure. A seismicity increase was observed in October 2017 by the IGEPN seismic array (20) coinciding with a rapid increase in EnKF models in shear failure using a cohesion value of C = 20 MPa as indicated by the vertical gray line. Six months prior to eruption initiation (C) is indicated by the black dotted line, and the timing of the eruption (D) is indicated by the red dashed line. (B) The percentage of models in the EnKF ensemble experiencing tensile failure along the reservoir boundary indicates that 80-90% of the models are experiencing reservoir tensile failure in the days prior to the eruption for tensile strength,  $Tc \ge 5$  MPa. (C) The calculated failure for the mean EnKF model on December 26, 2017. The cross-section runs south-north through the center of the pressure source. Colors represent calculated Andersonian fault orientations (38) in regions of predicted Mohr-Coulomb failure, cohesion, C =10 MPa. No tensile failure is predicted along the reservoir boundary, Tc = 1 MPa. (**D**) The calculated failure for the mean EnKF model on June 26, 2018. The black dashed outline on the southern wall of the reservoir indicates the region of calculated tensile failure along the reservoir boundary.



**Fig. 5.** Coulomb static stress transfer (30, 31) is calculated due to the 26 June 2018 Mw 5.4 earthquake, strike = 248, dip = 70 to the north, rake = 90, Young's modulus = 50 GPa, assuming receiver faults with strike = 105, dip = 70, rake = 90. (A) Cross section along X-X' indicated on (B) through the assumed earthquake source fault (white line) and the location of Fissure 1 ("F1"). The dashed black ellipse outlines the location of the pre-eruption forecast pressure source. The EnKF hindcast of Mohr-Coulomb failure (C = 1 MPa, gray outline), and tensile failure (green region) are shown for June 26, 2018. Dotted horizontal line indicates the 2 km-depth of the Coulomb stress change plotted in B. (B) Map view of Coulomb static stress transfer calculation at 2 km depth. Star symbol indicates the center of the forecasted pressure source that extends to the dashed, black outline. The white circle indicates the center of the hindcast source, with its full extent outlined by the white line.